Advanced Ti:Er:$LiNbO_3$ Waveguide Lasers

C. Becker, T. Oesselke, J. Pandavenes, R. Ricken, K. Rochhausen, G. Schreiber, W. Sohler, *Associate Member, IEEE*, H. Suche, *Associate Member, IEEE*, R. Wessel, S. Balsamo, I. Montrosset, *Member, IEEE*, and D. Sciancalepore

Invited Paper

***Abstract*—This paper reviews the latest developments of diode-pumped Ti:Er:$LiNbO_3$ waveguide lasers emitting at wavelengths around 1.5 μm. In particular, harmonically mode-locked lasers, Q-switched lasers, distributed Bragg reflector (DBR)-lasers, and self-frequency doubling lasers are discussed in detail. Supermode stabilized mode-locked lasers have been realized using a coupled cavity concept; a side mode suppression ratio of 55 dB has been achieved at 10-GHz pulse repetition rate with almost transform limited pulses. Q-switched lasers with a high extinction ratio ($>$25 dB) intracavity electrooptic switch emitted pulses with a peak power level up to 2.5 kW and a pulsewidth down to 2.1 ns at 1-kHz repetition frequency. Numerical simulations for both lasers are in a good, almost quantitative agreement with experimental results. A DBR-laser of narrow linewidth ($\approx$3 GHz) with a permanent (fixed) photorefractive grating and 5 mW output power has been realized. Self frequency doubling lasers have been fabricated with a periodic microdomain structure inside an Er-doped laser cavity; simultaneous emission at the fundamental wavelength, 1531 nm, and at the second harmonic wavelength, 765 nm, has been obtained.**

***Index Terms*—Distributed Bragg reflector lasers, erbium doping, frequency conversion, lithium niobate, mode-locked lasers, optical waveguides, photorefractive effect, Q-switched lasers.**

I. Introduction

In THE last few years, $LiNbO_3$ has gained much attention as a laser active material for integrated optics [1]. The ease of fabrication of low —loss erbium-diffusion doped Ti:$LiNbO_3$ channel guides has allowed the development of a whole new family of advanced laser devices of higher functionality thanks to the excellent electrooptic, acoustooptic, and nonlinear optical properties of the substrate. Besides loss compensated or even amplifying single- and double-pass devices [2], [3], waveguide lasers with intracavity monolithically integrated modulators, switches, and wavelength filters led to the demonstration of mode-locked [4], [5], Q-switched [6] and tunable lasers [7]. New enabling technologies like holographic writing and fixing of photorefractive gratings [8] and electric field assisted inversion of ferroelectric microdomains [9] led to the development of distributed Bragg reflector (DBR) and self-frequency doubling lasers [10], [11]. Moreover, the different types of lasers and amplifiers can be combined with other active and passive devices on the same substrate [12] to form integrated optical circuits (IOC's) for a variety of applications in optical communications, sensing, signal-processing, and measurement techniques.

It is the aim of this paper to review the latest developments of Ti:Er:$LiNbO_3$ integrated optical lasers. In Section II, harmonically mode-locked lasers are reported that utilize a coupled cavity design for a drastically improved pulse amplitude stability. In Section III, a very efficient actively Q-switched waveguide laser is discussed. The high extinction ratio of its intracavity electrooptic switch yields a high prelasing threshold and hence allows to generate pulses of very high peak power levels up to the kilowatt-range. DBR lasers with holographically written fixed photorefractive grating for narrow linewidth feedback are reported in Section IV. In Section V, we discuss results of the first self-frequency doubling Er-doped waveguide laser, which utilizes quasi-phase-matched optical second-harmonic generation in an intracavity Er-doped and periodically domain inverted waveguide structure. We conclude with a discussion of future prospects in this field.

II. Supermode Stabilized Mode-Locked Lasers

Compact and rugged pulse sources with repetition rates in the multigigahertz range become more and more important in particular for future optical communication systems. Therefore, frequency modulated (FM)-type mode-locked Ti:Er:$LiNbO_3$ waveguide lasers with an integrated travelling wave phase modulator as a mode locker have been developed and investigated [5], [13]. By harmonic mode locking, pulses up to 10-GHz repetition rate have been generated using approximately 7-cm-long devices to get the required pump absorption. However, harmonically mode-locked lasers usually emit more than one comb of longitudinal modes (called supermode) simultaneously, leading to high-frequency beat noise.

Several methods of supermode stabilization have been reported in the literature for fiber lasers with a very large number of supermodes. As one approach, an intracavity Fabry–Perot filter with a high finesse (>50) has been successfully used to

Manuscript received September 22, 1999; revised December 1, 1999 . This work was supported by the European Union with the ACTS Project ESTHER and by the VIGONI program, by the Heinz Nixdorf Institute, University of Paderborn, and the Deutsche Forschungsgemeinschaft with the Project "Integrated Optics in $LiNbO_3$.

C. Becker, J. Pandavenes, R. Ricken, K. Rochhausen, G. Schreiber, W. Sohler, H. Suche, and R. Wessel are with Angewandte Physik, Universität-GH Paderborn, Paderborn D-33098 Germany.

T. Oesselke was with Angewandte Physik, Universität-GH Paderborn, Paderborn D-33098 Germany. He is now with Lambda Physik, Göttingen, Germany

S. Balsamo and D. Sciancalepore are withPirelli Optical Systems S.p.A., 20126 Milan MI, Italy.

I. Montrosset iswith the Dipartimento di Elettronica, Politecnico di Torino, Turin 10129 Italy.

Publisher Item Identifier S 1077-260X(00)01566-5.

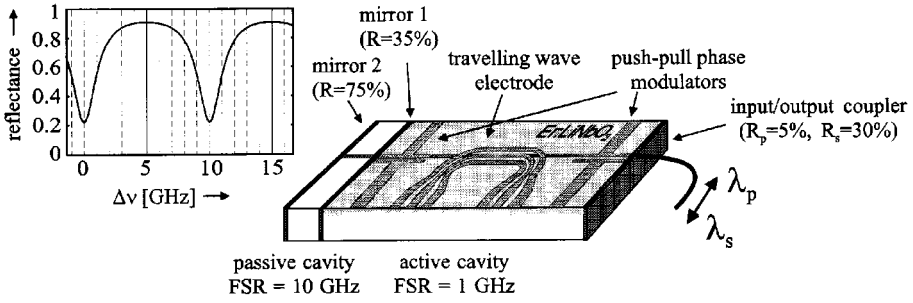

Fig. 1. Schematical diagram of the 10-GHz mode-locked Ti:Er:$LiNbO_3$-waveguide lasers with coupled cavity. Inset: calculated reflectance of the passive cavity versus relative optical frequency at the wavelength 1550 nm. Vertical lines: longitudinal modes of the stabilized supermode (solid) and of the suppressed supermodes (dashed).

select one supermode [14]. In contrast to this transmission-type filter, we recently reported supermode stabilization by coupling the active laser cavity directly to a passive Fabry–Perot waveguide cavity with a low finesse [15], [16]. In this way, a reflection-type filter was realized on the same substrate material with the potential for full integration. As shown in Fig. 1, a single supermode is selected by the reflectivity maxima of the passive cavity if the free spectral range (FSR) of the passive cavity is matched to the mode spacing of the supermodes.

Moreover, the integrated Fabry–Perot filter can also be used for repetition rate multiplication, as has been demonstrated with fiber lasers [17].

In the following, the fabrication, theoretical analysis, and properties of integrated, supermode stabilized mode-locked Ti:Er:$LiNbO_3$ lasers are presented.

A. Fabrication and Cavity Design

In order to fabricate the active laser cavity, a Z-cut $LiNbO_3$ substrate has been doped by indiffusion of a 30-nm-thick layer of vacuum-deposited Er at 1130 °C during 150 h. Afterwards, photolithographically defined 7-μm-wide and 96-nm-thick Ti-stripes have been indiffused at 1060 °C during 8.5 h to form the 66-mm-long active waveguides.

Prior to the electrode fabrication, a 0.9-μm-thick SiO_2-buffer layer has been vacuum deposited on the substrate surface to avoid excess losses. Three metal electrodes (see Fig. 1) have been fabricated on the laser structure using photolithographic liftoff of a sandwich of 30-nm sputtered Ti and 120-nm sputtered Au. Subsequently, the travelling-wave electrode was electroplated up to a thickness of 6 μm. The traveling-wave phase modulator in the middle of the cavity has a 25-mm-long symmetric coplanar microstrip line used for FM-type mode locking. Half-wave voltages of 6.6 V (π) and 25 V (σ) have been measured. At both ends of the active laser cavity, two lumped-type phase modulators have been integrated for push–pull operation to reduce spatial hole burning effects.

The mirrors of the active and the passive cavities have been deposited directly on the polished end faces by vacuum evaporation. The input/output coupler is designed as a low-pass filter and consists of 15 layers of SiO_2 and TiO_2. It has been fabricated with quarter-wave layers for 1900 nm, leading to a reflectivity at 1480 nm of about 5% and of 30% at 1550 nm wavelength. The mirrors of the passive cavity at the back side are broad-band reflectors of four layers ($R = 35\%$) and eight layers ($R = 75\%$), respectively, leading to a finesse of 4.3.

For supermode stabilization, the active waveguide resonator has been glued to the passive one (see Fig. 1) serving as a laser mirror with a frequency dependent reflectivity. The inset of Fig. 1 presents the calculated reflectivity of the passive cavity. The finesse of 4.3 has been chosen as a compromise between maximum output power in backward direction (high reflectivity and high finesse) and best supermode discrimination (low finesse).

The laser has been pigtailed with the common branch of a fiber-optic wavelength-division multiplexer (WDM). They were packaged in an Al-housing including temperature stabilization, an optical isolator, and two fiber-optic power splitters to get one output tap (1%) for monitoring and another one (9%) for deriving a control signal for feedback stabilization [13].

B. Theoretical Model

1) The Theoretical Model Foundation: The developed numerical model of mode-locked lasers summarized here is based on semiclassical laser theory [18] and has been presented in detail in [19]. It accurately describes the interaction of the laser signal with the active medium, which is responsible for the signal gain along the cavity, and with the electrooptic modulator, which is responsible for the coupling between the axial modes [20], [21].

Schematically, the model takes into account:

1) two-level system approximation with wavelength-dependent cross sections to describe the Er-ions;
2) overlap between transverse profile of the optical fields (pump and signal) and the active medium populations;
3) distributed interaction between the optical field and the travelling-wave phase modulator through the refractive index perturbation induced by the electrooptic effect;
4) single transverse mode field for signal and pump.

The time-dependent solution is represented as the superposition of the longitudinal cavity modes assuming a general shape for the optical pulse instead of the usual Gaussian approximation [21].

The generic complex field modal amplitude $e_n(t)$ satisfies the following differential equation:

$$\frac{de_n}{dt} + \left[\frac{1}{2}v\alpha_n^{\text{tot}} - j(\Omega_n - \omega_n)\right] e_n = -j\frac{1}{2}\mu_0 v^2 \omega_n \int\int [p_{G,n}(\vec{r}_t, t) + p_{\text{rf},n}(\vec{r}_t, t)]\Psi_s(\vec{r}_t)\, d\vec{r}_t \tag{1}$$

where $v = c/n$ is the phase velocity, μ_0 is the vacuum permeability, Ω_n and ω_n are the angular frequencies of the longitudinal modes of the unperturbed cavity (cold cavity) and active cavity, respectively, Ψ_s is the signal-mode intensity, $\vec{r}_t$ is the position in the transverse plane, and α_n^{tot} stands for total signal power losses, defined by the following equation:

$$\alpha_n^{\text{tot}} = \alpha_n^s + \frac{1}{2L}\ln\left(\frac{1}{R_l(\lambda_n)R_r(\lambda_n)}\right). \tag{2}$$

Here $R_l(\lambda_n)$ and $R_r(\lambda_n)$ are the nth signal power reflectivities of the left and right mirror, respectively, and α_n^s accounts for the waveguide losses. The terms on the right side of the (1) represent the coupling coefficients due to the gain and the RF phase modulation. These have been obtained by expressing the dielectric polarization P as a superposition of the longitudinal cavity modes

$$P(\vec{r}, t) = P_G(\vec{r}, t) + P_{\text{rf}}(\vec{r}, t) = \sum_n (p_{G,n}(\vec{r}_t, t) + p_{\text{rf},n}(\vec{r}_t, t))e^{j\omega_n t}U_n(z)\sqrt{\Psi}_s(\vec{r}_t) \tag{3}$$

where $U_n(z) = \sin(\beta_n z)$ is the standing-wave function and p_n is the complex polarization amplitude of the nth mode. P_G, due to the active medium, is represented with the classical expression

$$P_G(\vec{r}, t) = \epsilon_0 n^2 \chi_G(\vec{r}, t)E(\vec{r}, t) \tag{4}$$

where ϵ_0 is the vacuum dielectric permeability and E is the relevant component of the total electric field. The expression of the complex susceptibility $\chi_G = \chi_G' - j\chi_G''$, can be derived from semiclassical laser theory; in particular χ_G' has been neglected and χ_G'' is closely linked to the active medium gain and can be written in the quasi-two-level system approximation as

$$\chi_{G,n}'' = -\frac{nc}{\omega_n}\left[(\sigma_e^n + \sigma_a^n)N_2(\vec{r}, t) - \sigma_a^n N_0(\vec{r}, t)\right] \tag{5}$$

where $\sigma_{e,a}$ are the frequency-dependent emission and absorption cross sections and N_2 and N_0 represent the population densities of the upper and ground state of the Er-ions, respectively. N_2 has been developed in spatial longitudinal harmonics to take into account the standing-wave effect of the cavity modes

$$N_2(\vec{r}, t) \approx \gamma(\vec{r}_t)\left[n_{2,0}(t) + \sum_j n_{2,j}(t)\cos(2\beta_j z)\right] \tag{6}$$

where $\gamma(\vec{r}_t)$ takes into account the spatial transverse dependence of the upper level population, $n_{2,0}$ is the upper population level mean value along the longitudinal direction, and $n_{2,j}$ are the coefficients of the jth spatial harmonic with the period $2\beta_j = 4\pi j/L$, with L being the cavity length. The interaction between the optical field and the travelling-wave phase modulator has been included by considering the corresponding polarization P_{rf} representing the refractive index perturbation induced by the electrooptic effect

$$P_{\text{rf}}(\vec{r}, t) = -\epsilon_0 n^4 r E_{\text{rf}}(\vec{r}, t)E(\vec{r}, t) \tag{7}$$

where r is the relevant coefficient of the electrooptic tensor and $E_{\text{rf}}(\vec{r}, t)$ is the relevant component of the microwave field. Substituting in (1) and neglecting the rapidly varying terms, we obtain

$$\int\int p_{\text{rf},n}(\vec{r}_t, t)\Psi_s(\vec{r}_t)\, d\vec{r}_t = -\frac{2\epsilon_0 n^2}{\omega_n}X_n\delta_n[e_{n-1}e^{-j\phi} + e_{n+1}e^{j\phi}] \tag{8}$$

where

$$X_n = \frac{\omega_n n^2 r V_{\text{rf}}\Gamma}{4d}. \tag{9}$$

Here, V_{rf} is the applied voltage, d is the interelectrode distance, and Γ is the overlap integral between the transverse microwave and optical fields, while the other parameters (δ_n and ϕ) depend on the overlap of the longitudinal modal fields in the electrode region [18]. The coupling term in (8) shows how modes $(n-1)$ and $(n+1)$ are coupled with mode n and vice versa as a consequence of the phase modulation at a frequency around the cavity FSR.

Introducing the previous equations in (1) and choosing a suitable time origin, we obtain for the complex amplitude $e_n(t)$ of each longitudinal mode the following differential equation:

$$\frac{de_n}{dt} = \left[\frac{1}{2}v\left(g_n - \alpha_n^{\text{tot}}\right) + j(\Omega_n - \omega_n)\right] e_n + jX_n\delta_n\left[e_{n-1} + e_{n+1}\right]. \tag{10}$$

The system of modal equations (10) can be represented also in matrix form as

$$\frac{d\vec{e}}{dt} = -\underline{\underline{M}}\vec{e} \tag{11}$$

where $\vec{e} = [e_1, \ldots, e_{N_{\text{mode}}}]$ is the complex amplitude vector and the nonlinear matrix operator $\underline{\underline{M}}$ has a tridiagonal structure, with nonzero elements on the codiagonals. Last, for the dynamical evolution equation for the averaged absorbed pump power $P(t)$, we assumed the form

$$\frac{dP}{dt} = -v_p(\alpha_p + \alpha_p^{\text{Er}})P + v_p K P_{\text{inc}} \tag{12}$$

where α_p accounts for the waveguide losses for the pump, K is the coupling constant between the pump power inside the cavity and the incident pump power (P_{inc}), and α_p^{Er} is the pump absorption coefficient.

2) The Numerical Implementation: The steady-state behavior is studied by setting to zero the time derivatives; the solution is obtained by solving a set of homogeneous nonlinear coupled equations. The N_{mode} eigenvectors (with complex eigenvalues λ) of the matrix $\underline{\underline{M}}$ represent the N_{mode} possible

complex field configurations (supermodes; see Yariv *et al.* [22]). For each of them, the corresponding complex eigenvalue determines the steady-state behavior; the real part $\mathrm{Re}(\lambda)$) is the correction of the net gain of the supermode needed to reach the stable lasing condition, while the imaginary part ($\mathrm{Im}(\lambda)$) accounts for a central wavelength shift of the supermode. Neglecting statistical fluctuations, the lasing supermode characteristics are obtained from the analysis of the eigenvector whose eigenvalue satisfies first the condition $\mathrm{Re}(\lambda) = 0$.

3) Harmonic Mode-Locking Operation: The theoretical model presented above can be immediately extended to the case of harmonic mode locking by substituting the subscripts $(n-k)$ and $(n+k)$ for $(n-1)$ and $(n+1)$, where k is the order of the harmonics in (10). The pulse characteristics of each supermode in isolation can be obtained as for the case of fundamental mode locking. In the harmonic regime, an important point is the evaluation of the ratio of the powers between the lasing and the adjacent supermode [side-mode suppression ratio (SMSR)]. Starting from the equation

$$\frac{dP_i}{dt} = -\mathrm{Re}(\lambda_i)P_i + S_i \tag{13}$$

where P_i and S_i are the total stimulated and spontaneous emission powers associated to the ith supermode, we obtain

$$\mathrm{SMSR} = \frac{2P_0[\mathrm{Re}(\lambda_0) - \mathrm{Re}(\lambda_1)]}{S_1} \tag{14}$$

where the subscripts 0 and 1 refer to the lasing and to the adjacent supermode. This numerical model of harmonic mode locking has been extensively used to obtain a comparison with the experimental results. This comparison is reported and discussed in Section II-C.

C. Laser Performance

1) Operation Conditions: The stability of mode-locked lasers with Fabry–Perot-type cavities suffers from spatial hole burning effects, which degrade the low-frequency as well as the high-frequency stability. The holes in the population inversion are located at the cavity positions where the pulses are crossing each other ($n-1$ positions for nth harmonic mode locking) [23]. Therefore, the (push–pull) phase modulators close to the waveguide ends are used to shift the intensity pattern back and forth to suppress these standing-wave effects [24]. A push–pull modulation of about 5–MHz frequency and 0.1-rad modulation depth was sufficient to get rid of spatial hole burning effects.

In order to suppress relaxation spiking of the laser during mode locking, 9% of the laser output was detected and used for controlled pumping [13]. With a low-frequency (2-MHz bandwidth) stabilization unit, a correction component to the drive current of the pump laser diode was generated. It was possible to suppress the low-frequency noise by up to 42 dB.

For FM-type mode locking, the RF driver signal from a synthesizer has been boosted to an RF power of 26.5 dBm (σ-polarization) and 22.5 dBm (π-polarization), respectively. Mode locking was achieved at 9.93 GHz (σ) and 10.28 GHz (π). In contrast to fiber lasers, stable mode locking was possible without any active control of the optical cavity length [14].

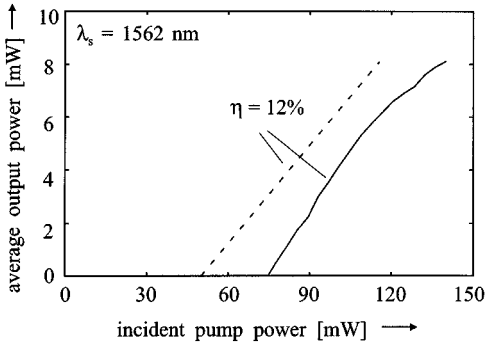

Fig. 2. Power characteristics of the 10-GHz mode-locked coupled cavity laser in σ-polarization. Solid line: measured; dashed line: calculated.

2) Power Characteristics: The mode-locked laser has been pumped by a broad-band high-power laser diode with a central wavelength of 1480 nm. Up to 140 mW of pump power was available in the common branch of the WDM in front of the waveguide laser. The laser emitted for σ-polarized (TE) pumping in σ-polarization at the wavelength of 1562 nm. The average output power of the laser during mode locking is shown in Fig. 2. A threshold of 74 mW and a slope efficiency of 12% have been measured, leading to a maximum average output power of more than 8 mW. In comparison with the single cavity laser (with a highly reflecting back-side mirror), the output power is reduced by 12%. For π-polarized pumping, the laser emitted in π-polarization at 1575 nm wavelength. A threshold of 90 mW and a maximum output power of 2.2 mW have been measured.

The dashed curve in Fig. 2 shows the calculated power characteristic. The same slope efficiency but a lower laser threshold of 50 mW have been calculated.

3) Supermode Selection: To investigate the supermode stability, the output pulses have been detected by a photodiode with 19 GHz bandwidth and analyzed by an RF spectrum analyzer. In Fig. 3, the results for different mode-locked lasers are compared. In a single cavity laser without supermode stabilization (a), strong supermode beat noise components with a frequency difference of the FSR ($\approx$1 GHz) are visible. An SMSR of only 8 dB has been measured.

The coupled cavity laser exhibits a drastically improved performance. In the RF spectrum of the σ-polarized output, only small beat components at 1, 2, 9, and 11 GHz appear, indicating that only the adjacent supermodes are not completely suppressed. Nevertheless, the supermode stability of this laser with an SMSR of 55 dB is excellent.

For the π-polarized output at 1575-nm wavelength, an SMSR of 45 dB has been achieved. These experimental results coincide well with the theoretical modeling results. Without supermode stabilization by a passive cavity, an SMSR of 10 dB has been calculated. For the coupled cavity laser, an SMSR of 45 dB has been obtained from the simulations (π-polarization). It is expected from the theoretical model and experimentally observed that the SMSR for mode locking in σ-polarization is higher than for π-polarization. This is due to a lower coupling coefficient of the spontaneous emission noise to the guided mode (compare (14)).

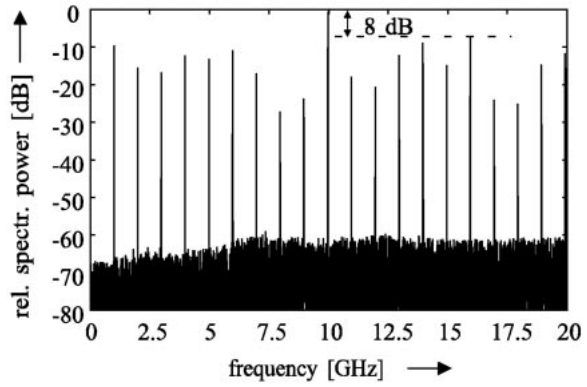

(a)

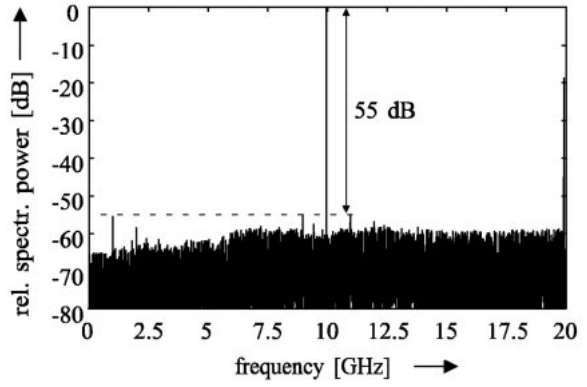

(b)

Fig. 3. RF spectrum at tenth harmonic mode locking of the σ-polarized output of the (a) single cavity laser and (b) coupled cavity laser. Resolution bandwidth: 10 kHz.

4) Pulse Properties and Detuning Characteristics: The laser emission has been investigated in more detail by measuring the autocorrelation of the optical pulses and the optical spectrum with a resolution of 0.015 nm. This has been done in the whole frequency range of several megahertz where stable mode locking is observed. The pulse properties for both polarizations are compared at the mode-locking frequencies where the smallest pulsewidths are obtained (set as zero detuning). For the σ-polarized output, a minimum pulsewidth of 5.7 ps and a spectral bandwidth of 0.64 nm have been measured, leading to a time bandwidth product of 0.45. This indicates that the pulse is almost chirp-free, if a Gaussian pulse shape is assumed. Due to the higher modulation index of the π-polarized signal, a smaller pulsewidth of 4.8 ps and a larger bandwidth of 0.87 nm have been measured. The time bandwidth product is slightly larger (0.50).

The highly resolved optical spectrum of the σ-polarized emission at zero detuning, presented in Fig. 4(a), shows the comb of longitudinal modes representing the selected supermode; the mode spacing is 0.081 nm. The stable emission of this spectrum confirms the excellent supermode stability.

From the literature, it is well known that FM-mode-locked lasers can suffer from pulse phase instabilities [21]. The pulse train of the laser is synchronized either to the phase modulation maximum (called positive mode) or to the phase modulation minimum (called negative mode). According to modeling results [21], [19], the central wavelength shifts to longer (shorter) wavelengths by increasing the RF driver frequency for the positive (negative) mode, respectively.

Fig. 4 presents a sequence of spectra of the σ-polarized emission, measured over an RF frequency tuning range of 3.8 MHz. Between -0.4 and 2.8 MHz detuning, the central wavelength was rising with the RF frequency, which means that the laser was emitting stably in the positive mode. This result coincides with the observation of the laser pulses using a fast sampling oscilloscope. No jumps between interleaved pulse trains occurred in this frequency range. For π-polarization, the laser emitted stably in the negative mode; the wavelength was decreasing with RF frequency.

For both polarizations, jumps of the central emission wavelength have been observed (e.g., 0.42 nm at 0.5-MHz detuning in Fig. 4). By accurately investigating the spectrum at these driver frequencies with a Fabry–Perot spectrum analyzer, it was found that the laser emission jumped from one supermode to the neighboring one: the comb of longitudinal modes displayed in Fig. 4 was shifted by one axial mode spacing ($\approx$1 GHz). These supermode jumps are caused by a slight mismatch between the FSR of the passive cavity and the tenth harmonic of the FSR of the active cavity (mode-locking frequency) of about 1%.

As is shown in Fig. 4, the pulsewidth of the σ-polarized output varies only from 5.7 to 7.8 ps within the detuning range from -0.4 to 2.8 MHz. Consequently, the time bandwidth product remains below 0.52. For the π-polarized output, the time bandwidth product remains below 0.57 within a larger detuning range of 4.2 MHz.

Using the theoretical model described in Section II-B, the detuning characteristic has been analyzed in detail for the σ-polarized emission. The laser has been found to emit on the positive mode in a 2.2-MHz detuning range. Outside of this frequency range, the negative mode has been selected from the model. The calculated pulsewidth is almost constant between 5.3 and 6.5 ps within the tuning range of the positive mode, in good accordance to the experimental results. Together with the calculated bandwidth of 0.88 nm, a time bandwidth product of 0.57 results for zero detuning. Due to the comparatively large bandwidth, the calculated time bandwidth product is larger than the experimental one.

The calculated central wavelength shift of the positive mode was 1.7 nm/MHz—significantly larger than the averaged measured shift (0.43 nm/MHz). However, it has been found that this central wavelength shift and the stability of the positive and negative modes depend strongly on the input parameters. In particular, the modeling results are very sensitive to small variations of the wavelength-dependent emission cross sections.

D. Pulse Repetition Rate Multiplication

Using the higher order sidebands of the intracavity FM modulation, the pulse repetition rate of actively mode-locked lasers can be multiplied by an integer multiple q of the modulation frequency. Two different arrangements are possible: For rational harmonic mode locking, the cavity is modulated with a frequency f_m/q, where f_m/q is not a multiple of the active cavity FSR but f_m is one. Therefore, longitudinal modes with a spacing of f_m are locked, and the pulse repetition rate is multiplied by a factor of q [25]. In another scheme, an

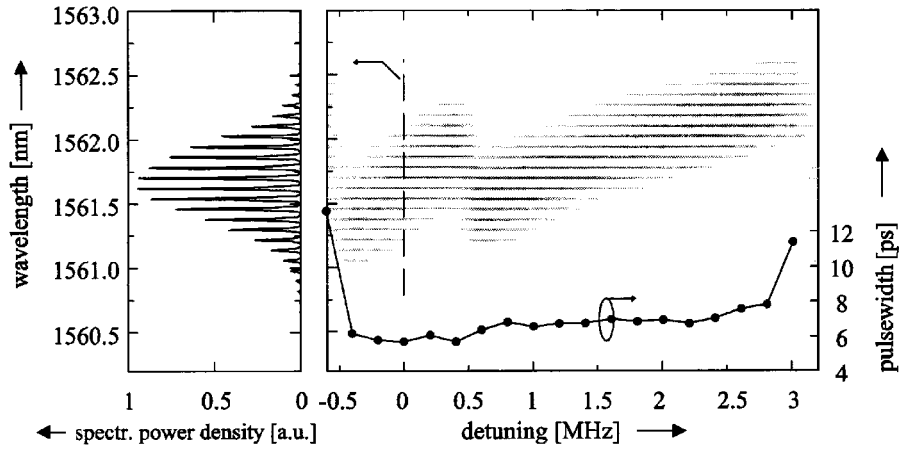

(a) (b)

Fig. 4. Detuning characteristics of the 10-GHz coupled cavity laser in σ-polarization. (a) Optical power density versus wavelength at the driver frequency of 9.9318 GHz (corresponding to zero detuning, marked with the dashed vertical line on the right). (b) Optical power density spectra and pulsewidths versus RF driver frequency detuning.

intracavity Fabry–Perot filter with an FSR of f_m is used to suppress the lower order FM sidebands (e.g., at f_m/q) [17].

Both schemes have been applied to the coupled cavity mode-locked Ti:Er:$LiNbO_3$ waveguide laser. For σ-polarization, pulse repetition rate multiplication (by factors of two, three, and four) has been achieved at frequencies of 4.965, 3.310, and 2.483 GHz with 30 dBm of RF power fed to the travelling-wave electrode, respectively. For π-polarization, twofold and fourfold multiplications of the pulse repetition rate have been obtained at driver frequencies of 5.142 and 2.571 GHz.

Five GHz is a multiple of the active cavity FSR. Therefore, the second method is used for frequency multiplication with the passive cavity as an intracavity filter. For both polarizations, low-noise pulse trains have been obtained—also for σ-polarization with a low round-trip phase modulation of 0.23 rad. Fig. 5 shows the RF spectrum and the pulse train of the σ-polarized output measured with a fast photodiode and a sampling scope. The 5-GHz RF component is 47 dB smaller than the signal at 10 GHz. The sampling oscilloscope trace indicates an excellent pulse stability.

The driver frequencies 3.3 and 2.5 GHz are not harmonics of 1 GHz (mode-locking frequencies of the active laser cavity). So mode locking at 10 GHz with these driver frequencies corresponds to rational harmonic mode locking. The passive filter cavity is used here—as before in the conventional mode-locked laser—for the supermode selection and stabilization. In contrast to the pulse-doubling scheme, a reduction of the output power has been observed, which is described also in [17]; it was about 10% for σ-polarization. Due to the higher threshold and the higher modulation index of the π-polarized laser emission, the laser operation was completely extinguished at 3.3-GHz phase modulation. For the fourfold multiplication in π, an optimum RF power level of 30.1 dBm has been found where the reduction of the output power (15%) is minimized. The autocorrelation of the pulse train measured at this power level and the threefold and fourfold multiplication of the σ-polarized output are shown in Fig. 6. The pulsewidth of the π-polarization at

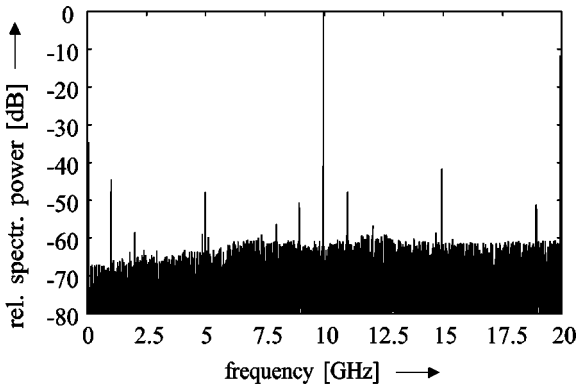

(a)

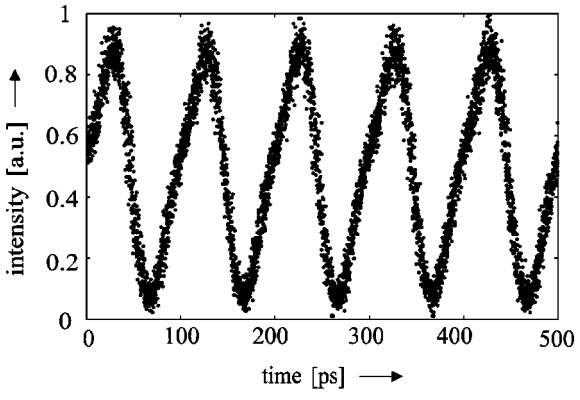

(b)

Fig. 5. (a) RF spectrum and (b) sampling oscilloscope trace of the detector response for the σ-polarized, pulse repetition rate doubled, mode-locked laser operation.

2.5-GHz modulation was clearly smaller (10 ps) than the pulses of the σ-polarized output. As expected from the theory given in [17], pulse phase instabilities of the 10-GHz pulse train (that means jumping by 50 ps) occurred only for the 3.3- and not for the 2.5- and 5-GHz modulations.

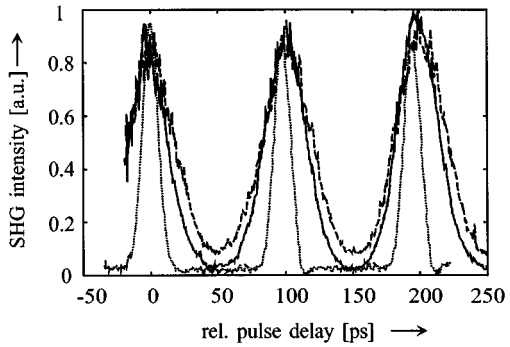

Fig. 6. Autocorrelation traces of the pulse train for a driver frequency of 3.31 GHz (σ, solid line), 2.48 GHz (σ, dashed line), and 2.57 GHz (π, dotted line).

This method can be used for generating pulse trains for high-capacity communication systems, e.g., pulse repetition rates of 40 GHz using drive signals of 10 GHz only.

III. High-Power Actively Q-Switched Lasers

Diode-pumped integrated Q-switched lasers can be efficient, miniaturized sources of short optical pulses with a variety of possible applications. They could be used as pump sources for parametric nonlinear frequency conversion, as sources for optical time-domain reflectometry (OTDR) and for laser based range finding. For the latter application, eye safe sources are recommended. Er-doped Q-switched lasers emitting at about 1.55-μm wavelength meet this requirement and have therefore attracted increasing attention in the last years [26]–[28]. High Er-concentration levels up to the solid solubility limit can be achieved by indiffusion without significant fluorescence quenching. This feature together with the long fluorescence lifetime of the Er-ions guarantee a high energy storage capability and a high power conversion efficiency, which can be exploited for the design of efficient Q-switched waveguide lasers. Peak power levels in the kilowatt range have been predicted [27]. Moreover, due to the excellent electrooptic properties of the $LiNbO_3$ substrate, the required intracavity switch can be monolithically integrated [29], leading to a compact and rugged laser design.

A. Fabrication

The structure of the device and the setup for its operation are schematically shown in Fig. 7.

The total length L of the laser is 75 mm. Half (with respect to the X-direction) of the Z-cut (Y-propagation) $LiNbO_3$ substrate has been doped over the complete length near the surface by indiffusion of 30 nm of vacuum deposited Er at 1130 °C during 150 h. Subsequently, the photolithographically defined 7-μm-wide and 100-nm-thick Ti-stripes have been indiffused at 1060 °C during 7.5 h to form the optical waveguide structure of the laser. In the undoped region, waveguide scattering losses of 0.03 dB/cm have been measured. The large improvement of the actual laser compared to the one reported earlier [28] is due to the intracavity electrooptic switch of high extinction ratio. It has been realized as a folded (by the rear cavity mirror) Mach–Zehnder-type interferometer with a highly symmetric Y-junction as the power splitter. This Y-junction with

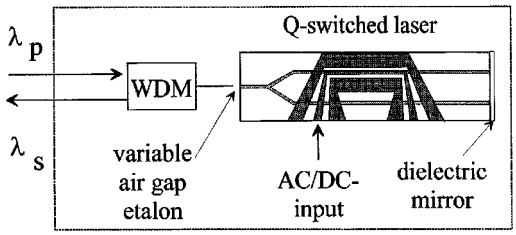

Fig. 7. Schematical sketch of the laser structure and the experimental setup for the investigation of Q-switched laser operation.

X-sine shaped bends is located in the center of the cavity. Its excess loss is about 0.15 dB, and its deviation from a symmetrical power splitting is below 0.2 dB, leading to an estimated modulator extinction ratio of better than −25 dB. This prevents, as predicted by the numerical simulation, CW-prelasing up to the maximum available pump power.

On the waveguide structure, a 0.6-μm-thick insulating SiO_2-buffer has been vacuum deposited prior to the electrode fabrication. The electrode structure of the intracavity modulator (Q-switch) is a 25-mm-long symmetric coplanar microstrip line fabricated by liftoff of a sandwich of sputtered Ti/Au. The modulator has been operated as a lumped device without low resistance termination due to the relaxed bandwidth requirements. The halfwave voltage for the laser polarization TE-(σ-) is about 14 V due to the smaller electrooptic coefficient available in this polarization. The laser has a Fabry–Perot cavity composed of a dielectric mirror vacuum deposited on the rear waveguide end faces and a variable etalon with air gap (see Fig. 7). The dielectric mirror has a high reflectance (98%) at both emission wavelength ($\lambda_s \approx 1562$ nm, σ-polarized, or $\lambda_s \approx 1575$ nm, π-polarized) and pump wavelength ($\lambda_p \approx 1480$ nm). In this way, double-pass pumping is provided, allowing an improved pump absorption efficiency. On the other side, an output/pump coupler mirror has been realized by an air gap etalon formed by the end faces of the pump input/signal output fiber (common branch) of the WDM and the polished Ti:Er:$LiNbO_3$-waveguide end face. The effective reflectance of this mirror has been adjusted such that the pump experiences minimum coupling losses and the resonated laser field "sees" the maximum reflectivity of about 0.3. With this design, fully packaged and pigtailed lasers have been realized.

B. Theoretical Model

A dynamic model and the corresponding numerical code to simulate the behavior of such a Q-switched waveguide laser have been developed. The model is based on the following hypothesis.

1) The Er:$LiNbO_3$ system has been approximated as a quasi-two-level-system with wavelength-dependent absorption and emission cross sections.
2) Gain and loss coefficients are calculated using overlap integrals of the population inversion density of the involved Er-levels with the corresponding transverse signal and pump intensity distributions, respectively. A mean field approach (spatial averaging over the longitudinal intensity distributions [30]) leaving only time-dependent gain and loss coefficients is applied to reduce the complexity

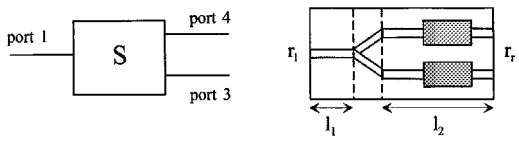

(a) (b)

Fig. 8. (a) Y-junction as three port device described by S-matrix. (b) Schematical layout of the laser with indicated section lengths and reflectors.

of the final equations to evaluate the temporal evolutions of the pump and signal mode powers.

3) Three different rate equations have been used to approximate the population inversion density in the different parts of the folded MZ cavity. The system of $N_{\mathrm{mode}}+4$ (inversion density in the three sections plus pump evolution) coupled nonlinear differential equations has been solved numerically with an adaptive time-step routine suitable for stiff systems.

The branched resonator [see Fig. 8(b)] characteristics are obtained through a resonance condition involving the S-matrix coefficients S_{ij} $(i=1, j=3,4)$ of the power splitter for arbitrary splitting ratio and the mirror reflectivities.

We define an equivalent power gain coefficient g_{eq} of the nth cavity mode, which takes into account the amplitude modulation due to a time-dependent phase shift $2\Delta\phi(t)$ in one or both (push–pull) branches of the folded intracavity Mach–Zehnder interferometer

$$g_{\mathrm{eq}} = g_1\frac{l_1}{L} + \frac{1}{L}\ln\left(S_{13}^2 e^{g_3 l_2} + S_{14}^2 e^{g_4 l_2}\right) = g_1\frac{l_1}{L} + g. \quad (15)$$

l_1 and l_2 denote the lengths of the single- and dual-channel sections, respectively, with $l_1 + l_2 = L$ (total cavity length). g_1 is the gain coefficient of the single-channel section and $g_{3,4}$ are those of the two branches of the dual-channel section, respectively.

The overall gain per round trip can be expressed as follows:

$$G = R_1 R_2 e^{2g_1 l_1}\left(S_{13}^2 e^{g_3 l_2} + S_{14}^2 e^{g_4 l_2}\right)^2 \cdot\left\{1 - 4S_{13}^2 S_{14}^2 e^{[(g_3+g_4)l_2 - 2gL]}\sin^2\Delta\phi(t)\right\}. \quad (16)$$

$R_{1,2}$ denote the reflectivities of the two cavity mirrors. An additional simulator for continuous-wave (CW) operation allows one to check the lasing wavelength and to compare the CW power with the average power during Q switching predicted by the dynamic simulator.

The highest output power is predicted for σ-polarized pump and signal radiations. This has been confirmed by the experimental results. For low cavity losses ($\leq$0.15 dB/cm), the lasing wavelength is generally 1562 nm, while for higher losses, 1531-nm emission prevails.

The splitting-dependent extinction ratio of the folded Mach–Zehnder interferometer is expected to determine the CW prelasing threshold. For the optimum polarization, splitting asymmetries as large as 30:70% do not result in prelasing up to a launched pump power of about 140 mW.

The influence of the ratio l_1/l_2 is more pronounced on the pulse peak power than on the pulsewidth. For 50% output coupling, a variation from $l_1/l_2 = 5/1$ to $l_1/l_2 = 1/5$ results in a 20% increase of the peak power but only a 10% increase in the pulse duration.

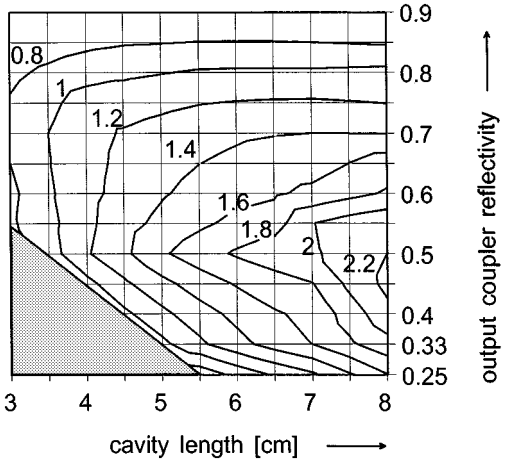

Fig. 9. Contour plot of constant peak power in kilowatts in a plane: cavity length versus output coupler reflectivity; the emission wavelength is 1562 nm except in the shaded area, where it is 1531 nm.

In Fig. 9, lines of constant peak output power at 1562-nm wavelength for 1-kHz pulse repetition rate and 0.15-dB/cm waveguide attenuation at both signal and pump wavelengths are given in a contour plot as function of the cavity length and the output coupler reflectance. A pump power of 150 mW and a ratio $l_1/l_2 = 1/5$ have been assumed.

As confirmed by the CW simulator, the laser emission wavelength is 1562 nm throughout the whole plot except the gray shaded area, where the emission wavelength changes to 1531 nm. There is a pronounced maximum of the output power with respect to the output coupling but not with respect to the cavity length, at least within the chosen range of 80 mm, which is close to the present technical limit (4-in substrates). The best performance of a 7.5-cm-long laser of 2.1 kW peak power and 3.7-ns pulsewidth [full-width at half-maximum (FWHM)] is predicted for 55% output coupler reflectivity. For the same output coupler, the maximum peak power of 2.6 kW with respect to the cavity length was found for 12 cm. A similar behavior can be obtained for different single to dual channel ratios. The experimental results shown in Fig. 10(a) for an output coupler reflectivity of about 0.3 and a cavity length of 75 mm agree very well with the simulation results shown in Fig.9 and—as a function of time—in Fig. 10(b).

C. Laser Performance

Using a pigtailed laser diode ($\lambda_p \approx 1480$ nm) of up to 145 mW output power as the pump source, a threshold of about 90 mW (σ-polarized) has been achieved for σ-polarized emission at 1562-nm wavelength. The modulator has been operated with a dc-bias voltage to give maximum optical extinction and an ac-switching voltage (square wave) of amplitude V_π and about 5% duty cycle in the frequency range 1–5 kHz. No evidence of prelasing has been identified. The Q-switched pulses have been attenuated by about 50 dB in a cascade of fiber-optic splitters and attenuators to ensure linearity of the detector, a biased PIN photodiode of 1.5 GHz bandwidth. The detector signal has been measured using a scope of again 1.5-GHz bandwidth. In Fig. 10,

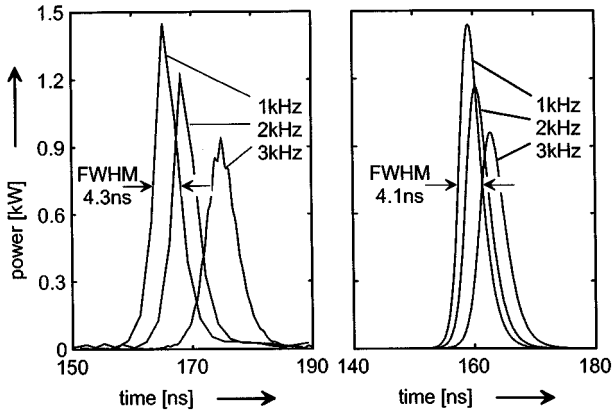

(a) (b)

Fig. 10. Output power of a Q-switched Ti:Er:$LiNbO_3$-waveguide laser versus time; the zero of the abscissa scale coincides with the leading edge of the electrical switching pulse; parameter of the set of graphs is the pulse repetition frequency. (a) Measured results and (b) simulated results.

experimental (a) and theoretical (b) results of Q-switched operation of the Ti:Er:$LiNbO_3$ waveguide laser are presented for 145 mW incident pump power. The zero point of the abscissa of the diagrams corresponds to the leading edge of the electrical switching pulse. At 1 kHz repetition rate, up to 1.44 kW peak power has been measured. The buildup time is about 165 ns, and the pulsewidth is 4.3 ns (FWHM) [6]. With increasing repetition rate, the peak power degrades and the pulsewidth and the buildup time increase, respectively. A good, quantitative agreement between measured and calculated peak power levels and pulsewidths has been achieved.

With lasers of even smaller waveguide losses, we have recently achieved pulse peak power levels of about 2.5 kW. High-resolution scans of these pulses clearly show a fine structure (burst of pulses) with a periodicity identical to the round trip time in the laser cavity. We attribute this to self-mode-locking. Such intense, short pulses would allow very high temporal resolution, e.g., in OTDR applications.

For π-polarized pumping π-polarized emission at 1575 nm has been observed with significantly lower peak powers (up to $\simeq$500 W) compared to the σ-polarized emission at 1562 nm wavelength.

IV. Photorefractive Grating DBR Lasers

Recently, integrated optical Ti:Er:$LiNbO_3$ DBR lasers were developed with holographically defined ion-beam-etched surface gratings for narrow-band optical feedback. Their emission wavelength is determined by the periodicity of the grating. Even single frequency operation has been obtained [31].

However, DBR lasers with etched surface gratings suffer from several drawbacks: The fabrication technology is complicated [32]. Grating inhomogeneities induce extra losses of the lasing mode. The overlap of the grating and the lasing mode is very small, requiring a long interaction length. The pump mode is partially coupled to substrate modes resulting in high extra losses; therefore, pumping through the Bragg grating is not possible.

Photorefractive gratings, as successfully used in fiber-optic DBR and distributed feedback lasers [33], are a very promising alternative to etched gratings, avoiding all the drawbacks mentioned above. In the following, a DBR-waveguide laser ($\lambda = 1531$ nm) in Er-diffusion-doped $LiNbO_3$ with a fixed photorefractive grating in an Fe-doped Ti-diffused strip waveguide is described [10]; the device has been pumped by a laser diode.

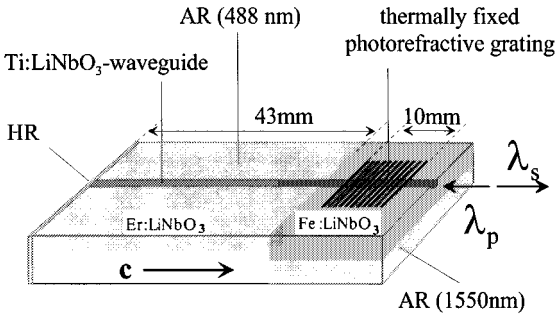

Fig. 11. Schematical structure of the Ti:Er:$LiNbO_3$ DBR waveguide laser with photorefractive grating in the Fe-doped section. HR: Highly reflecting dielectric mirror. AR: Antireflection coating.

A. Fabrication and Grating Characterization

A schematic diagram of the laser is presented in Fig. 11. It was fabricated in a 70-mm-long X-cut $LiNbO_3$ substrate, which has been Er-doped over 43 mm by an indiffusion of a 15-nm-thick, vacuum-deposited Er-layer at 1120 °C during 120 h. Subsequently, the remaining surface was Fe-diffusion doped (33 nm, 1060 °C, 72 h) to increase the photorefractive sensitivity for grating fabrication. Last, a 8-μm-wide, 97-nm-thick, photolithographically defined Ti-stripe parallel to the c-axis has been indiffused forming the optical channel guide. The sample has been annealed at 500 °C for 3 h in flowing Ar (0.5 L/min) to enhance the Fe^{2+}/Fe^{3+}-ratio, which determines the photorefractive sensitivity.

The laser resonator consists of a broad-band dielectric high reflector on the polished waveguide end face of the Er-doped section and of the narrow-band grating reflector in the Fe-doped section. The end face on the right-hand side has been antireflection (AR) coated for fiber butt coupling. Last, the upper and lower sample surfaces have been AR-coated as well to avoid interference effects during the grating fabrication.

The grating has been written using a holographic setup with an Ar-laser ($\lambda = 488$ nm). The periodic illumination leads to a corresponding excitation of electrons from Fe^{2+}-states; they are redistributed by drift, diffusion, and the photovoltaic effect in $LiNbO_3$. The last named is the dominant transport mechanism along the optical c-axis. The electrons are trapped by acceptor states (Fe^{3+}-ions) in areas of low optical intensity. This redistribution generates a periodic space charge field, which modulates the refractive index via the electrooptic effect and in this way generates a narrow-band Bragg-reflector grating.

A grating fabricated at room temperature is not stable. Therefore, it has been written by a 2-h exposure at 170 °C. At this temperature, protons in the crystal become mobile and compensate the periodic electronic space charge [34], [8]. After cooling to room temperature, these ions are frozen at their high-temperature positions. Homogeneous illumination with the collimated beam of a 100-W halide lamp then leads to a nearly homogeneous redistribution of the electronic charge, developing in this

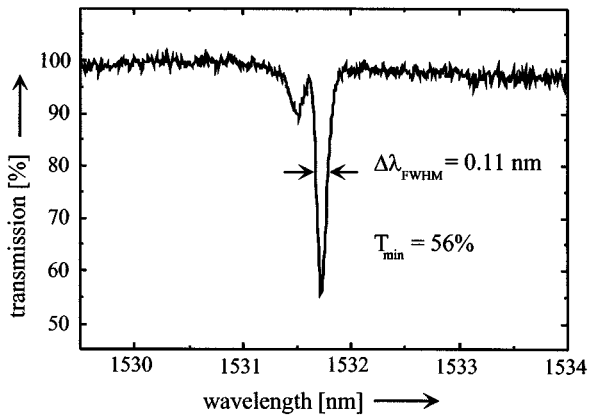

Fig. 12. Transmission of the fixed photorefractive grating versus wavelength.

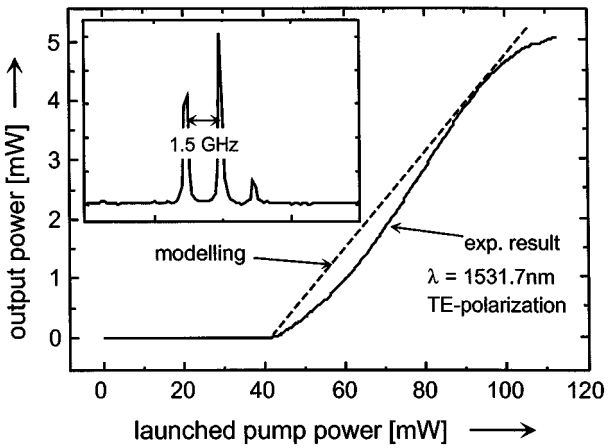

Fig. 13. Power characteristics of the DBR laser. Inset: axial mode spectrum (TE-polarized).

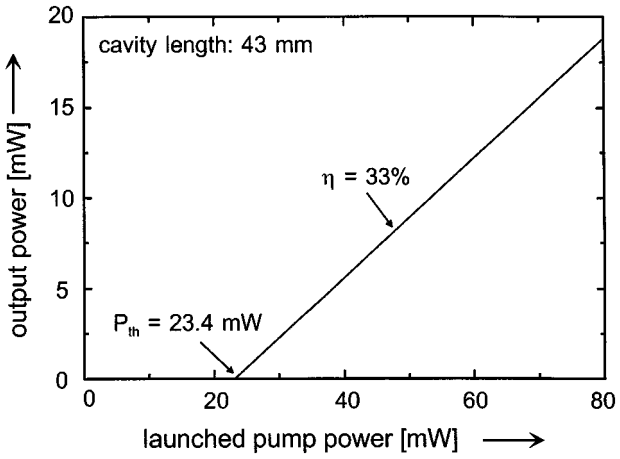

Fig. 14. Calculated power characteristics of an optimized DBR laser (emission wavelength: 1560 nm).

way a stable ionic grating as a replica of inverse polarity of the initial electronic space charge distribution.

The spectral characteristics of the holographically written gratings have been determined by slightly pumping the device and measuring the backscattered amplified spontaneous emission from the Er-doped section transmitted through the grating. This yielded a minimum transmission of about 40%, corresponding to a reflectivity of about 60%. However, due to a finite dark conductivity for electrons, the fixed ionic grating is slowly compensated as a function of time, resulting in a corresponding reflectivity decrease. Fig. 12 shows the specific result measured approximately 3 h after grating fabrication; the reflectivity of about 44% yields optimum output coupling of the DBR-laser cavity. The halfwidth of the grating response is about 0.11 nm.

Fortunately, it is easy to develop the grating again by another homogeneous illumination. We demonstrated that even commercially available GaN-LED's are well suited to recover the grating response (and in this way the DBR-laser emission) within approximately 1 h; continuous illumination then keeps the reflectivity and the laser output power constant.

B. Laser Performance

To operate the DBR laser, a pigtailed diode laser ($\lambda_p \approx 1480$ nm) has been used for pumping. A fiber-optic WDM launched up to 110 mW of pump power into the DBR laser and simultaneously extracted the laser emission in backward direction. Laser emission has been achieved in both TE- and TM-polarization. TE-polarization for both pump and emission has yielded the maximum output power (see Fig. 13), as the smaller TE-modes result in a better overlap with the Er concentration profile. To suppress TM-emission, a stripe of Ag paste operating as a TE-pass polarizer has been deposited across the waveguide close to the high reflector. The grating bandwidth of $\simeq$0.11 nm has led to the simultaneous emission of three longitudinal modes (see inset of Fig. 13) with a central wavelength of 1531.7 nm. The maximum TE-polarized output power of 5 mW has been measured for a grating reflectivity of about 45%. The saturation of the output power at high pump power levels was due to a change of the pump spectrum (broadening and shifting to longer wavelengths) caused by back reflections into the nonisolated diode laser. As a result, the pump absorption efficiency and hence the slope efficiency of the DBR-laser were reduced.

Modeling results predict a significant potential for improvements. Assuming 0.1 dB/cm waveguide scattering losses, an optimized Er-concentration profile and output coupling through the grating, up to 32% slope efficiency and 15 mW output power at 80 mW of launched pump power seem to be feasible at the same emission wavelength ($\lambda = 1531.7$ nm). Even better results can be expected at longer wavelengths; as an example, Fig. 14 presents the calculated characteristics for $\lambda = 1560$ nm.

V. Quasi-Phase-Matched Self-Frequency Doubling Lasers

Very recently, periodic poling of Ti:Er:$LiNbO_3$ waveguides was demonstrated for the first time [11]. This is a key result, as it opens the possibility to combine different types of waveguide lasers with quasi-phase-matched nonlinear frequency converters even in the same waveguide structure. The latter can be second-harmonic, difference and sum-frequency-generators, parametric amplifiers, and oscillators. A whole new class of laser active frequency converting devices can be designed. Examples are self-frequency doubling lasers and optical parametric oscillators with intracavity pump laser. However,

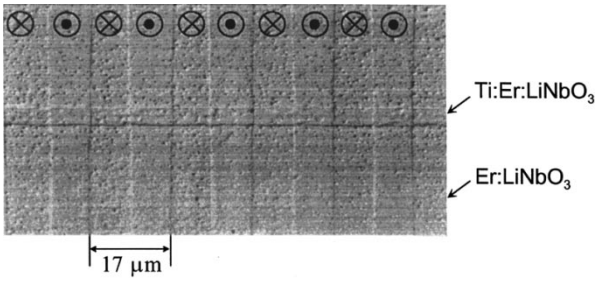

Fig. 15. Chemically etched surface of a periodically poled Ti:Er:$LiNbO_3$ optical waveguide.

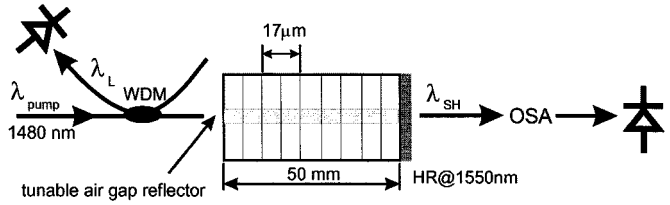

Fig. 16. Schematic diagram of the experimental setup to investigate the self-frequency doubling Ti:Er:$LiNbO_3$ waveguide laser (OSA: optical spectrum analyzer).

up to now only self-frequency doubling lasers have been developed [11]. Fabrication and properties are reported in the next sections.

A. Fabrication

The laser has been fabricated in a 50-mm-long, Z-cut, 0.5-mm-thick $LiNbO_3$ substrate. First, an Er-layer of 28-nm thickness, vacuum deposited on the $(-Z)$-face, was indiffused (1130 °C/150 h). Afterwards, 98-nm-thick and 7-µm-wide Ti-stripes were photolithographically defined parallel to the crystal X-axis and indiffused (1060 °C/7.5 h) in the Er-doped surface to form the optical waveguides. A shallow domain inverted layer, generated on the $(+Z)$-side of the substrate during the diffusion processes, had to be removed by mechanical grinding. Subsequently, the domain orientation of the substrate as a whole was inverted by electric field poling followed by periodic poling using a photoresist grating of 17-μm period on top of the waveguide as mask for a liquid electrolyte electrode. In this way, a better uniformity of the periodic domain structure in the waveguide was achieved, as domain growth during the poling process always starts at the $(+Z)$-face. Fig. 15 shows a photograph of the etched surface of an Er-doped periodically poled waveguide. No significant differences of the quality of the domain pattern of doped and undoped samples were observed.

B. Laser Operation and Performance

A fiber-optic WDM was used to couple up to 135 mW of pump radiation at 1480 nm center wavelength from a laser diode into the Ti:Er:$LiNbO_3$ waveguide resonator (see Fig. 16). The input mirror was a tunable, low finesse Fabry–Perot etalon, formed by the end face of the optical fiber and the polished, uncoated front face of the waveguide. The fiber was mounted on a piezo-driven translator allowing to adjust the thickness of the air gap and in this way the effective (wavelength dependent)

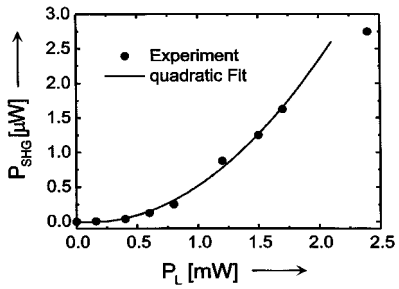

Fig. 17. SH power ($\lambda_{\rm SH} = 765.5$ nm) generated in forward direction as function of the fundamental laser power ($\lambda_L = 1531$ nm) emitted in backward direction.

reflectivity of the etalon between 5% and 30% (tunable air gap reflector). Due to its wavelength dependence, the preferred laser wavelength has been selected among emission at λ_L of 1531, 1545, 1575, and 1602 nm. The output mirror was a dielectric multilayer (12 layers), vacuum deposited on the polished rear waveguide end face, with a broad-band reflectivity of 95% in the wavelength range 1480 nm $< \lambda <$ 1800 nm. Around 765 nm the mirror transmission was high, exceeding 80%. The laser fundamental power was monitored in backward direction behind the WDM. In case of second-harmonic generation (SHG), the corresponding output power was measured in forward direction using an optical spectrum analyzer (OSA) as wavelength filter.

$\lambda_L = 1531$ nm was adjusted as the laser emission wavelength to allow quasi-phase-matched SHG in the periodically poled waveguide of 17-μm periodicity (at room temperature). In this configuration, the laser threshold was 87 mW coupled pump power. Due to waveguide and coupling losses, the slope efficiency was poor, allowing only up to 2.4 mW of output power. Simultaneously, frequency doubled radiation $\lambda_{\rm SH} = 765.5$ nm was generated in both forward and backward directions. Only the part emitted in forward direction was measured using an OSA to suppress the green upconversion light generated in the Er-doped waveguide. Up to 2.7 μW of SH power was emitted with a quadratic dependence on the fundamental laser power (see Fig. 17).

To improve the performance of the laser and to increase the SH-output power, a narrow bandwidth fiber Bragg grating has been used replacing the "air gap reflector." In this way, the fundamental wavelength is determined by the grating periodicity, the laser threshold is reduced, and the intracavity fundamental field strength is enhanced, leading to a higher SH-conversion efficiency. It was possible to increase the SH-output power by nearly one order of magnitude. In the future, even photorefractive Bragg gratings in the Ti:$LiNbO_3$ waveguides might be used [10] to develop a self-frequency doubling DBR laser.

VI. Conclusion

In conclusion, we have reviewed the recent progress in the field of Ti:Er:$LiNbO_3$ waveguide lasers. There is still a large potential to improve the properties of the different types of lasers significantly and to use them in selected applications. In particular, the repetition rate of the harmonically mode-locked laser can be increased to directly meet, without optical time division

multiplexing [35], the requirement of future fiber-optic communication systems of $\geq$40-Gb/s data rates. Their relatively high pulse peak power would allow one to excite optical solitons in fibers without any further amplification. The Q-switched laser is currently announced as a product for applications such as distance measurement and collision avoidance sensing [36]. The narrow linewidth DBR laser can be easily combined with other components on the same chip like external modulators or interferometers. Moreover, it should be possible to monolithically integrate more than one DBR laser with external modulator for WDM applications. Last, the self-frequency-doubling laser might become of interest as a pump source for cascaded nonlinear optical difference frequency generation as used in low-noise wavelength converters for optical communications in the 1.55-μm window. Besides extracavity, also intracavity combinations of lasers with quasi-phase-matched parametric devices like a self-pumped integrated optical parametric oscillator are demanding goals for the future.

REFERENCES

[1] I. Baumann, S. Bosso, R. Brinkmann, R. Corsini, M. Dinand, A. Greiner, K. Schäfer, J. Söchtig, W. Sohler, H. Suche, and R. Wessel, "Er-doped integrated optical devices in $LiNbO_3$," *IEEE J. Select. Topics Quantum Electron.*, vol. 2, pp. 355–366, June 1996.

[2] H. Suche, D. Hiller, I. Baumann, and W. Sohler, "Integrated optical spectrum analyzer with internal gain," *IEEE Photon. Technol. Lett.*, vol. 7, pp. 505–507, May 1995.

[3] R. Brinkmann, M. Dinand, I. Baumann, C. Harizi, W. Sohler, and H. Suche, "Acoustically tunable wavelength filter with gain," *IEEE Photon. Technol. Lett.*, vol. 6, pp. 519–521, Apr. 1994.

[4] H. Suche, I. Baumann, D. Hiller, and W. Sohler, "Modelocked Er:Ti:$LiNbO_3$—Waveguide laser," *Electron. Lett.*, vol. 29, no. 12, pp. 1111–1112, 1993.

[5] H. Suche, R. Wessel, S. Westenhofer, W. Sohler, S. Bosso, C. Carmannini, and R. Corsini, "Harmonically modelocked Ti:Er:$LiNbO_3$—Waveguide laser," *Opt. Lett.*, vol. 20, no. 6, pp. 596–598, 1995.

[6] H. Suche, T. Oesselke, J. Pandavenes, R. Ricken, K. Rochhausen, W. Sohler, S. Balsamo, I. Montrosset, and K. K. Wong, "Efficient Q-switched Ti:Er:$LiNbO_3$ waveguide laser," *Electron. Lett.*, vol. 34, no. 12, pp. 1228–1229, 1998.

[7] I. Baumann, D. Johlen, W. Sohler, H. Suche, and F. Tian, "Acoustically tunable Ti:Er:$LiNbO_3$—Waveguide laser," in *Proc. 20th Eur. Conf. Optical Communication (ECOC'94)*, vol. 4, Florence, Italy, 1994, pp. 99–102.

[8] K. Buse, S. Breer, K. Peithmann, S. Kapphan, M. Gao, and E. Krätzig, "Origin of thermal fixing in photorefractive lithium niobate crystals," *Phys. Rev. B*, vol. 56, no. 3, pp. 1225–1235, 1997.

[9] M. Yamada, N. Nada, M. Saitoh, and K. Watanabe, "First-order quasiphase matched $LiNbO_3$ waveguide periodically poled by applying an external field for efficient blue second-harmonic generation," *Appl. Phys. Lett.*, vol. 62, no. 5, pp. 435–436, 1993.

[10] C. Becker, A. Greiner, T. Oesselke, A. Pape, W. Sohler, and H. Suche, "Integrated optical Ti:Er:$LiNbO_3$ distributed Bragg reflector laser with a fixed photorefractive grating," *Opt. Lett.*, vol. 23, no. 15, pp. 1194–1196, 1998.

[11] G. Schreiber, K. Rochhausen, R. Ricken, and W. Sohler, "Self-frequency doubling waveguide laser," in *Novel Lasers and Devices—Basic Aspects 1999*. Washington, DC: Opt. Soc. Amer., 1999, pp. 147–149. paper LWA9.

[12] W. Sohler, "Integrated optical circuits with Er$LiNbO_3$ amplifiers and lasers," in *Optical Fiber Communication Conf.* Washington, DC: Opt. Soc. Amer., 1996, vol. 2, p. 251.

[13] H. Suche, A. Greiner, W. Qiu, R. Wessel, and W. Sohler, "Integrated optical Ti:Er:$LiNbO_3$ soliton source," *IEEE J. Quantum Electron.*, vol. 33, pp. 1642–1646, Oct. 1997.

[14] J. S. Wey, J. G. Goldhar, and G. L. Burdge, "Active harmonic modelocking of an erbium fiber laser with intracavity Fabry-Perot filters," *J. Lightwave Technol.*, vol. 15, pp. 1171–1180, July 1997.

[15] R. Wessel, K. Rochhausen, H. Suche, and W. Sohler, "Single supermode harmonically modelocked Ti:Er:$LiNbO_3$ waveguide laser," in *Proc. CLEO/Eur.'98 in Glasgow*, 1998. postdeadline paper CPD1.5.

[16] R. Wessel, K. Rochhausen, R. Ricken, H. Suche, and W. Sohler, "10 GHz modelocked Ti:Er:$LiNbO_3$ waveguide laser with coupled cavity: Supermode selection and pulse repetition rate doubling," in *Proc. 9th Eur. Conf. Integrated Optics (ECIO'99)*, Torino, Italy, 1999, pp. 289–292.

[17] K. Abedin, N. Onodera, and M. Hyodo, "Higher order FM mode locking for pulse-repetition-rate enhancement in actively mode-locked lasers: Theory and experiment," *IEEE J. Quantum Electron.*, vol. 35, pp. 875–890, June 1999.

[18] W. H. Louisell, *Quantum Statistical Properties of Radiation*. New York: Wiley, 1973.

[19] D. Sciancalepore, S. Balsamo, and I. Montrosset, "Theoretical modeling of FM mode locking in Er,Ti:$LiNbO_3$ waveguide lasers," *IEEE J. Quantum Electron.*, vol. 35, pp. 400–409, Mar. 1999.

[20] S. E. Harris and O. P. McDuff, "Theory of FM laser oscillation," *IEEE J. Quantum Electron.*, vol. QE-1, pp. 245–262, June 1965.

[21] D. J. Kuizenga and A. E. Siegman, "FM and AM mode locking of the homogeneous laser—Part I: Theory," *IEEE J. Quantum Electron.*, vol. QE-6, pp. 694–708, Nov, 1970.

[22] R. A. Salvatore, S. Sanders, Th. Schrans, and A. Yariv, "Supermodes of high-repetition-rate passively mode-locked semiconductor lasers," *IEEE J. Quantum Electron.*, vol. 32, pp. 941–952, June 1996.

[23] M. Becker, D. Kuizenga, and A. Siegman, "Harmonic modelocking of the Nd:YAG laser," *IEEE J. Quantum Electron.*, vol. QE-8, pp. 687–693, Aug. 1972.

[24] H. Sabert and R. Ulrich, "Spatial hole burning in Nd^{3+}-fiber lasers suppressed by push-pull phase modulation," *Appl. Phys. Lett.*, vol. 58, no. 21, pp. 2323–2325, 1991.

[25] N. Onodera, A. J. Lowery, L. Zhai, Z. Ahmed, and R. S. Tucker, "Frequency multiplication in actively mode-locked semiconductor lasers," *Appl. Phys. Lett.*, vol. 62, no. 12, pp. 1329–1331, 1993.

[26] A. Yeniay, J.-M. P. Delavaux, J. Toulouse, D. Barbier, T. A. Strasser, J. R. Pedrazanni, and W. Minford, "Hybrid Q-switched laser with Ti-indiffused $LiNbO_3$ and Er-Yb Co-doped glass waveguides," *IEEE Photon. Technol. Lett.*, vol. 9, pp. 1580–1582, Dec. 1997.

[27] D. L. Veasey, J. M. Gary, J. Amin, and J. A. Aust, "Time-dependent modeling of erbium-doped waveguide lasers in lithium niobate pumped at 980 and 1480 nm," *IEEE J. Quantum Electron.*, vol. 33, pp. 1647–1662, Oct. 1997.

[28] S. Balsamo, S. Maio, I. Montrosset, H. Suche, and W. Sohler, "Q-switched Ti:Er:$LiNbO_3$ waveguide laser," *Opt. Quantum Electron.*, vol. 31, pp. 29–33, 1999.

[29] E. Lallier, D. Papillon, J. P. Pocholle, M. Papuchon, M. de Micheli, and D. B. Ostrowsky, "Short pulse, high power Q-switched Nd:MgO:$LiNbO_3$ waveguide laser," *Electron. Lett.*, vol. 29, no. 2, pp. 175–176, 1993.

[30] M. Dinand and W. Sohler, "Theoretical modeling of optical amplification in Er-doped Ti:$LiNbO_3$ waveguides," *IEEE J. Quantum Electron.*, vol. 30, pp. 1267–1276, May 1994.

[31] J. Söchtig, R. Gross, I. Baumann, W. Sohler, H. Schütz, and R. Widmer, "DBR waveguide laser in erbium-diffusion-doped $LiNbO_3$," *Electron. Lett.*, vol. 31, no. 7, pp. 551–552, 1995.

[32] J. Söchtig, H. Schütz, R. Widmer, R. Lehmann, and R. Gross, "Grating reflectors for erbium-doped lithium niobate waveguide lasers," in *Proc. SPIE Nanofabrication and Device Integration*, vol. 2213, 1994, pp. 98–107.

[33] J. Hübner, P. Varming, and M. Kristensen, "Five wavelength DFB fiber laser source for WDM systems," *Electron. Lett.*, vol. 33, no. 2, pp. 139–140, 1997.

[34] J. J. Amodei and D. L. Staebler, "Holographic pattern fixing in electro-optic crystals," *Appl. Phys. Lett.*, vol. 18, pp. 540–542, 1971.

[35] S. Hinz, D. Sandel, M. Yoshida-Dierolf, V. Mirvoda, R. Noé, G. Feise, H. Herrmann, R. Ricken, W. Sohler, H. Suche, F. Wehrmann, and R. Wessel, "Polarization mode dispersion compensation for 6 ps, 40 Gbit/s pulses using distributed equalisers in $LiNbO_3$," *Electron. Lett.*, vol. 35, no. 14, pp. 1185–1186, 1999.

[36] "Product announcement and preliminary data sheet," IMRA of America, Inc., 1999.

C. Becker was born in Olsberg, Germany, in 1970. He received the diploma degree in physics from the University of Paderborn, Germany in 1997.

His thesis dealt with the realization of a Ti:Er:Fe:$LiNbO_3$ DBR waveguide-laser with a holographically written grating.

T. Oesselke was born in Brakel, Germany, in 1972. He received the diploma degree in physics from the University of Paderborn, Germany, in 1997.

The topic of his thesis was the generation of thermally fixed photorefractive Bragg gratings in Ti:Fe:$LiNbO_3$-strip waveguides. He then joined Lambda Physik, Göttingen, Germany.

J. Pandavenes was born in Oviedo, Spain, in 1971. He received the Trabajo de Investigación degree in physics from the University of Oviedo in 1997.

He joined the Department of Applied Physics, University of Paderborn, Germany, in 1997, where he has been engaged in research on integrated optical modulators and erbium-doped Q-switched waveguide lasers in lithium niobate.

R. Ricken received the Dipl.-Phys. degree in physics from the University of Essen, Germany, in 1982.

He joined the Applied Physics group, University of Paderborn, Germany, in 1983. Since then, he has been responsible for the technology of integrated optical devices in lithium niobate.

K. Rochhausen received the Dipl.-Phys. degree in physics from the University of Paderborn, Germany, in 1997.

She is currently a Member of Technical Staff with the Applied Physics group, University of Paderborn, working on technology and fabrication of integrated optical circuits in lithium niobate.

G. Schreiber was born in Stockach/Baden, Germany, in 1969. He received the diploma degree in physics from the University of Konstanz, Germany, in 1995.

His diploma thesis was on atom lithography. In 1996, he joined the Department of Applied Physics, University of Paderborn, Germany. Since then, he has been working on optical frequency converters in periodically poled Ti:$LiNbO_3$ waveguides.

W. Sohler (A'88) was born in Wangen/Allgäu, Germany, in 1945. He received the Dipl.-Phys. and Dr.rer.nat. degrees in physics from the University of Munich, Germany, in 1970 and 1974, respectively.

From 1975 to 1980, he was with the University of Dortmund, Germany, working on integrated optics. In 1980, he joined the Fraunhofer Institut für Physikalische Messtechnik, Freiburg, Germany, as Head of the Department of Fiber Optics. Since 1982, he has been with the University of Paderborn, Germany, as a Professor of applied physics. His research interests include integrated optics, fiber optics, nonlinear optics, and laser physics. He is a coauthor of more than 150 journal contributions and several book chapters. He has been a member of the program committee of several (international) conferences on integrated optics.

Dr. Sohler is a member of the German Physical Society and the German Society of Applied Optics.

H. Suche (A'95) was born in Neukirchen/Sachsen, Germany, in 1951. He received the Dipl.-Phys. and Dr.rer.nat.-degrees in physics from the University of Dortmund, Germany, in 1978 and 1981, respectively.

His Ph.D. thesis was on integrated optical parametric oscillators in $LiNbO_3$. In 1981, he joined the Fraunhofer Institut für Physikalische Messtechnik, Freiburg, Germany, as a Research Member in the Department of Fiber Optics. Since 1982, he has been with the University of Paderborn, Germany, as Akademischer Oberrat within the Applied Physics group. His research interests include nonlinear integrated optics and laser physics. He currently works on active (Er-doped) integrated optical devices in $LiNbO_3$. H. Suche is a coauthor of more than 50 journal and conference contributions and of several book chapters.

Dr. Suche is a member of the German Physical Society.

R. Wessel was born in Paderborn, Germany, in 1969. He received the diploma degree in physics from the University of Paderborn in 1994.

In 1995, he joined the Department of Applied Physics of the University of Paderborn. There he is engaged in the development of mode-locked Ti:Er:$LiNbO_3$ waveguide lasers.

Mr. Wessel is a member of the German Physical Society.

S. Balsamo was born in Torino, Italy, on June 24, 1971. He received the Laurea and Ph.D. degrees in electronics engineering from Politecnico di Torino, Italy, in 1995 and 1999, respectively.

His research interests concern design, modeling, and characterization of optoelectronic devices; especially semiconductor lasers, semiconductor optical amplifiers, and solid-state (lithium niobate and Nd:YAG) lasers.

I. Montrosset (M'92) was born in Aosta, Italy, on November 19, 1946. He received the Laurea degree in electronics engineering from Politecnico di Torino, Italy, in 1971.

From 1972 to 1986, he was with the Department of Electronics, Politecnico di Torino, where in 1982 he became an Associate Professor. From 1986 to 1989, he was a Professor at Universit di Genova, Italy. Currently, he is a Professor of Optoelectronics at the Politecnico di Torino. Since 1984, he has been mainly involved in numerical simulations and design of guided-wave optics and optoelectronic devices.

D. Sciancalepore was born in Torino, Italy, on August 10, 1970. He received the Laurea degree in electronics engineering from Politecnico di Torino, Italy, in 1995.

His main interests are the design, modeling, and characterization of active and passive $LiNbO_3$ components.